ADVANCED MATERIALS
www.advmat.de

Atomic Iridium Incorporated in Cobalt Hydroxide for Efficient Oxygen Evolution Catalysis in Neutral Electrolyte

Youkui Zhang, Chuanqiang Wu, Hongliang Jiang, Yunxiang Lin, Hengjie Liu, Qun He, Shuangming Chen, Tao Duan, and Li Song**

Developing highly efficient catalysts for oxygen evolution reaction (OER) in neutral media is extremely crucial for microbial electrolysis cells and electrochemical CO_2 reduction. Herein, a facile one-step approach is developed to synthesize a new type of well-dispersed iridium (Ir) incorporated cobalt-based hydroxide nanosheets (nominated as CoIr) for OER. The Ir species as clusters and single atoms are incorporated into the defect-rich hydroxide nanosheets through the formation of rich Co–Ir species, as revealed by systematic synchrotron radiation based X-ray spectroscopic characterizations combining with high-angle annular dark-field scanning transmission electron microscopy measurement. The optimized CoIr with 9.7 wt% Ir content displays highly efficient OER catalytic performance with an overpotential of 373 mV to achieve the current density of 10 mA cm^{-2} in 1.0 M phosphate buffer solution, significantly outperforming the commercial IrO_2 catalysts. Further characterizations toward the catalyst after undergoing OER process indicate that unique Co oxyhydroxide and high valence Ir species with low-coordination structure are formed due to the high oxidation potentials, which authentically contributes to superior OER performance. This work not only provides a state-of-the-art OER catalyst in neutral media but also unravels the root of the excellent performance based on efficient structural identifications.

Electrochemical water splitting is expected to be a promising chemical process as the solution to the increasing fossil fuel depletion.[1–3] For two half-reactions in water splitting cells, oxygen evolution reaction (OER) at the anode has been regarded as the main bottleneck due to the sluggish kinetics and large overpotential.[4–7] With this regard, great efforts have been devoted to developing efficient electrocatalysts to accelerate the OER with reduced overpotential, thus improving the energy conversion efficiencies.[8–13] Recently, the first-row transition-metal-based catalysts, especially Co, Ni, and Fe-based materials, have attracted extensive attention and been developed as promising electrocatalysts for OER in alkaline media.[14–16] Moreover, the Co-based materials have also been reported to act as excellent catalysts for photo/electrocatalytic water oxidation.[17–19] Nevertheless, for OER in alkaline media, the corrosion of high-concentration alkaline electrolyte hinders their large-scale practical applications.[20] In this case, the neutral media is considered as environmental friendly electrolyte which can avoid the corrosion issue and reduce the cost of electrochemical system.[21–23] Furthermore, OER in neutral media is an important half-reaction for fascinating electrochemical CO_2 reduction reactions.[24] However, as reported so far, the overpotential of the anodic OER in neutral electrolytes is very high, and most of the reported OER catalysts are tested on the supports of Ti mesh or Au foam.[21,22,25] This surely limits the electrode type for the practical applications. Therefore, it is of great importance to break through the barrier of high overpotential via highly efficient OER electrocatalyst which can be operated in neutral media. On the other hand, OER-induced catalyst reconstructions are extensively observed due to the high anodic oxidation potentials.[26] Therefore, identifying the fine structure of reconstruction-derived component is highly desirable to shed light on the root of catalytic performance, but still keeping as a great challenge.

Herein, we demonstrate a facile chemical route to synthesize self-assembled 3D Co-based hydroxide hierarchical structures with Ir incorporation as highly active OER electrocatalyst. The as-synthesized products were elaborately characterized by synchrotron radiation based X-ray absorption fine structure (XAFS) spectroscopy and aberration-corrected atomic-resolution high-angle annular dark-field scanning transmission electron microscopy (HAADF-STEM), and the results revealing the composition of well-dispersed Ir atoms and ultrathin Co-based hydroxide nanosheets as subunits (marked as CoIr-*x*, *x* corresponding to the Ir/Co molar ratio in precursor). When the products were applied as the OER catalysts, the catalytic activities and stabilities were evaluated and compared through employing the commercial IrO_2 as the reference sample; and the excellent performance outperforming the IrO_2 in both neutral and alkaline conditions were delivered. Specially, the

Y. Zhang, C. Wu, Dr. H. Jiang, Y. Lin, H. Liu, Q. He, Dr. S. Chen, Prof. L. Song
National Synchrotron Radiation Laboratory
CAS Center for Excellence in Nanoscience
University of Science and Technology of China
Hefei 230029, China
E-mail: jhlworld@ustc.edu.cn; song2012@ustc.edu.cn
Y. Zhang, Prof. T. Duan
School of National Defense Science and Technology
Southwest University of Science and Technology
Mianyang 621010, China
The ORCID identification number(s) for the author(s) of this article can be found under https://doi.org/10.1002/adma.201707522.

DOI: 10.1002/adma.201707522

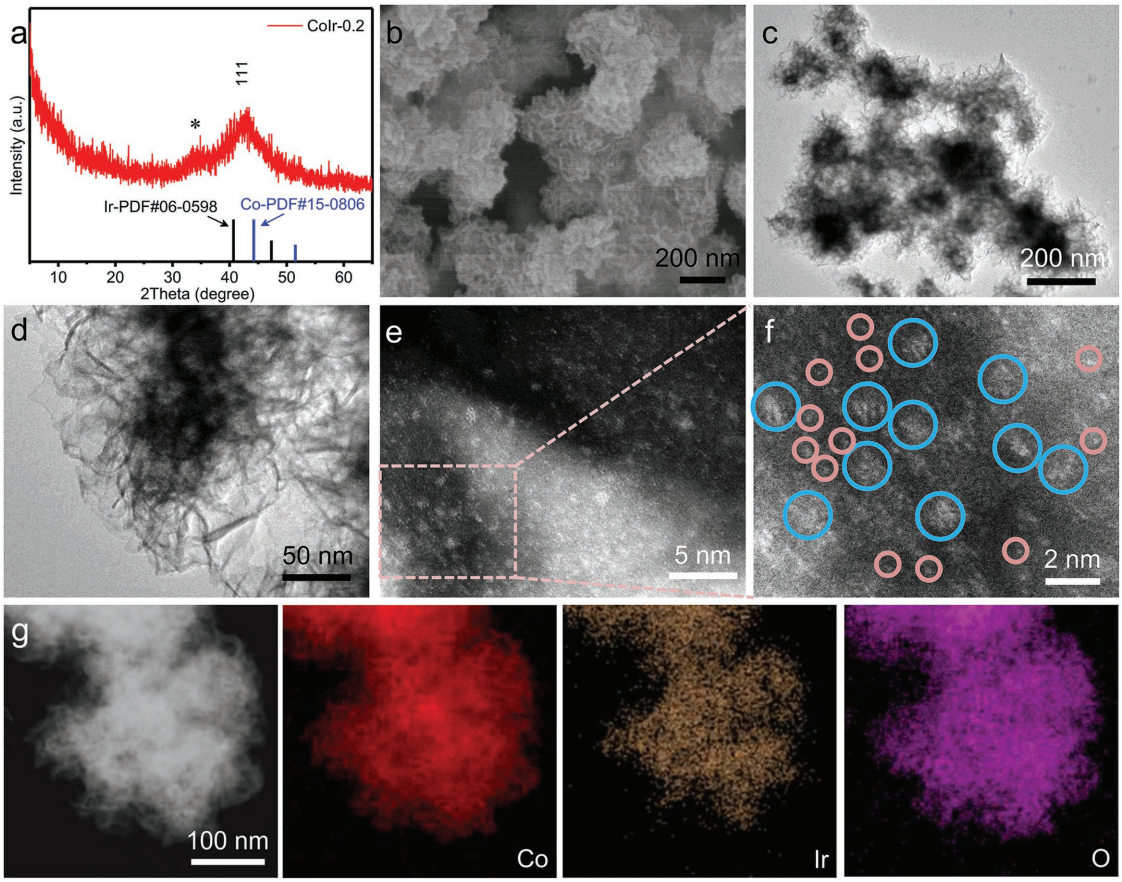

Figure 1. a) XRD pattern, b) SEM, and c,d) TEM images of CoIr-0.2. e,f) HAADF-STEM images of CoIr-0.2, with clusters of Ir marked in blue circles and single atoms of Ir highlighted in pink circles. g) Dark-field TEM image of CoIr-0.2 and the corresponding elemental mapping of Co, Ir, and O, respectively. The asterisk (*) in (a) represents the (012) reflection of α-$Co(OH)_2$.

structural characterization toward reconstruction-derived component was also conducted to identify the fine structure by X-ray absorption near-edge structure (XANES) and extended X-ray absorption fine structure (EXAFS) measurements.

In this work, the self-assembled 3D CoIr-*x* hierarchical structures were synthesized though a one-step reduction approach using $NaBH_4$ as reduction agent (see the Experimental Section for details). The powder X-ray diffraction (XRD) measurements were first carried out to verify the crystalline structures of various synthesized CoIr-*x* samples (**Figure 1** and Figure S1, Supporting Information). As shown in Figure 1a, the XRD pattern of CoIr-0.2 hierarchical structure shows one obvious broad peak at around 43°, which locates between the (111) plane of face-centered cubic (fcc) Ir (powder diffraction file (PDF) No. 06-0598) and (111) plane of fcc Co (PDF No. 15-0806), implying that Ir might be alloyed with Co and formed Co–Ir species.[27–29] For comparison, all the well-defined diffraction peaks of the product without Ir^{3+} adding (denoted as CoIr-0) fit well with the α-$Co(OH)_2$ (PDF No. 46-0605), which can be identified as (003), (006), (012), and (110) plane reflections (Figure S1, Supporting Information).[30] The detailed morphology and structure features of the as-prepared samples were observed by the field emission scanning electron microscopy (SEM) and transmission electron microscopy (TEM). The typical SEM and TEM images of CoIr-*x* clearly reveal that the nearly spherical 3D hierarchical structures are consisted of graphene-like flexible ultrathin nanosheets (Figure 1b–d and Figures S2–S4, Supporting Information). The ultrathin structure can maximally expose the active sites and promote the electrocatalytic properties. Through comparing the SEM and TEM images of the as-prepared samples, the average diameter of the spherical hierarchical structures decreases from ≈2 µm of CoIr-0 to ≈150 nm of CoIr-0.2 with the increasing of Ir concentration, suggesting that the Ir incorporation can restrict the growth of α-$Co(OH)_2$. When the Ir concentration was further increased, Ir nanoparticles were formed (as confirmed by high resolution TEM (HRTEM) for CoIr-0.3, Figure S5, Supporting Information). Besides, the HAADF-STEM images clearly show that the bright spots corresponding to Ir atoms are uniformly anchored into CoIr-0.2 hierarchical structure (Figure 1e,f), which can be divided into two types of Ir species including atomically anchored Ir single atoms and Ir clusters (marked in Figure 1f). The uniformly anchored Ir species can maximize the exposure of the active sites and provide abundant Ir sites for the bonding with Co atoms in α-$Co(OH)_2$ nanosheets to form Co–Ir species. In addition, the element mapping analysis indicates the homogeneous distribution of Ir species throughout the self-assembled 3D CoIr-0.2 hierarchical structure (Figure 1g and Figure S6, Supporting Information). The actual Ir loading in CoIr-0.05, CoIr-0.1, and CoIr-0.2 were 3.1, 5.6, and 9.7 wt%, respectively, obtained by inductively coupled plasma-mass spectrometry analysis.

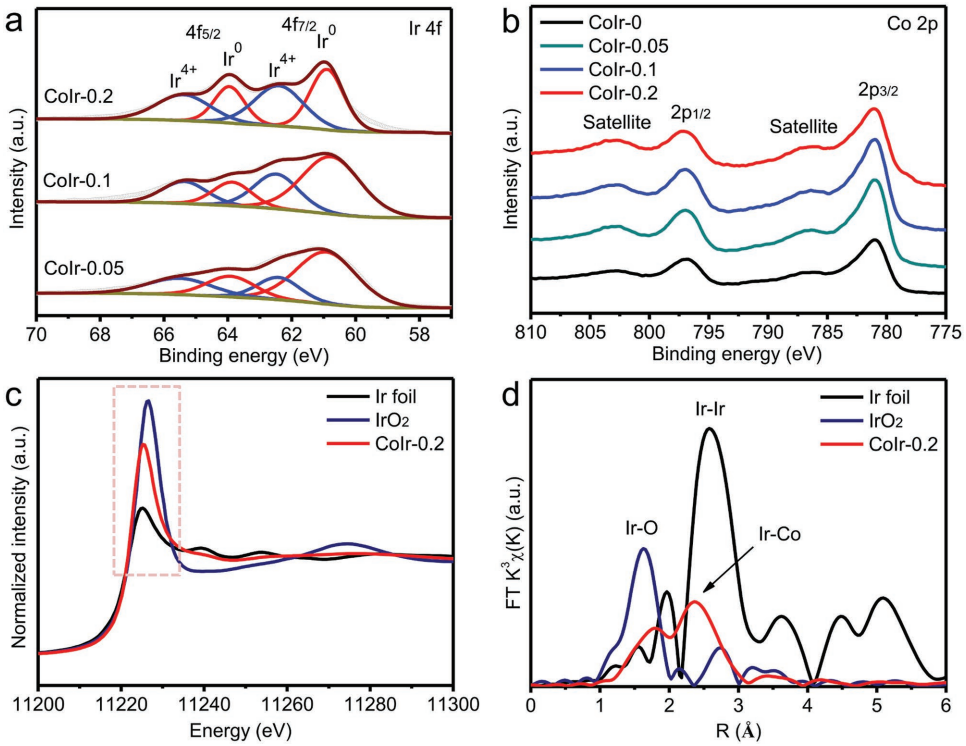

Figure 2. a) The Ir 4f and b) Co 2p core levels spectra of the CoIr-*x* samples. c) The Ir L_3-edge XANES spectra of CoIr-0.2 sample and the standard reference Ir and IrO_2 and d) the corresponding FT curves of the Ir L_3-edge EXAFS spectrum.

In order to identify the surface chemical composition and valence state information of the self-assembled CoIr-*x* hierarchical structures, X-ray photoelectron spectroscopy (XPS) was conducted. The high-resolution Ir 4f XPS spectrum of CoIr-*x* can be splitted into four peaks at 60.9, 62.4, 63.8, and 65.5 eV, corresponding to the binding energies of Ir^0 $4f_{7/2}$, Ir^{4+} $4f_{7/2}$, Ir^0 $4f_{5/2}$, and Ir^{4+} $4f_{5/2}$, respectively (**Figure 2**a),[31,32] indicating that Ir^0 and Ir^{4+} are coexistence in CoIr-*x* which will be further explored in the following section. The high-resolution Co 2p XPS spectrum of CoIr-*x* exhibits two main peaks located at the binding energies around 781 and 797 eV with two shakeup satellite peaks corresponding to the characteristic peaks of Co $2p_{3/2}$ and Co $2p_{1/2}$ orbit levels (Figure 2b), respectively, in good agreement with the state of Co in α-$Co(OH)_2$.[33] Besides, the high-resolution O 1s XPS spectrum can be deconvoluted into three characteristic peaks at 529.4 eV for oxygen atoms bound to metals, 531.3 eV for metal hydroxide belong to α-$Co(OH)_2$, and 532.4 eV for hydroxyl groups or surface-adsorbed oxygen (Figure S7, Supporting Information).[34]

To further give an in-depth identification of the local coordination structure of Ir species in the as-prepared CoIr-*x* hierarchical structures, XAFS measurement was performed. As shown in Figure 2c, the intensity of the white line of the normalized XANES spectrum at Ir L_3-edge of CoIr-0.2 is obviously lower than that of the standard reference IrO_2 but higher than that of reference Ir foil, indicating the coexistence of Ir^0 species and positively charged Ir species,[35] which is consistent with the XPS results. The corresponding Fourier transform (FT) curve of the Ir L_3-edge for CoIr-0.2 in *R* space was used to confirm the local geometry structure of the center Ir (Figure 2d). It should be noted that the FT curve of CoIr-0.2 is obviously different from the reference samples, suggesting the different arrangement of the Ir atoms. The major peak for CoIr-0.2 at about 2.38 Å can be corresponded to the formation of Co—Ir bond, which is longer than that of Ir—O bond (1.63 Å) in IrO_2 but shorter than that of Ir—Ir bond (2.58 Å) in Ir foil. Similar results can be found in previously reported Ir–Ni alloy and Ru–Co clusters.[36,37] This result indicates that the Co—Ir species are formed in the CoIr-*x* hierarchical structures, which is in good agreement with the XRD results. Besides, the FT curves of CoIr-0 and CoIr-0.2 in Co K-edge exhibit two main characteristic peaks of the Co—O and Co—Co coordinations, corresponding to the bulk α-$Co(OH)_2$ at 1.55 and 2.78 Å (Figure S8, Supporting Information), respectively, indicating that the as-prepared CoIr-*x* are mainly kept as α-$Co(OH)_2$ framework structure, which is in consistent with the XRD and XPS results. Upon Ir incorporated into Co hydroxide, a new coordination peak (marked with A) located at 2.16 Å is apparent in the Co K-edge FT curves, which is most likely correlated with the Ir incorporation. Moreover, compared with that of the bulk α-$Co(OH)_2$, the peak intensities of the ultrathin CoIr-0 and CoIr-0.2 nanosheets are decreased and shifted to low *R* (2.70 Å) by 0.08 at 2.78 Å (Figure S8, Supporting Information). The shifting of the peak to the low *R* can be attributed to the shorten of length of the Co—Co bond which is exposed on the surface of the ultrathin CoIr-*x* nanosheets.[38] The obviously decreasing of the peak intensities for CoIr-0.2 indicate that a large amount of surface Co atoms are not fully coordinated, which is accompanied by a large amount of defect formation.[38] By combining HAADF-STEM, XPS, and XAFS techniques, the atomic Ir species have been

identified unequivocally. Subsequently, these as-synthesized catalysts with different Ir concentrations were tested for OER.

The electrocatalysts with high OER performance under neutral condition is expected to be highly imperative for the renewable energy.[20,24] Thus, the electrocatalytic OER performance of the as-prepared 3D CoIr-*x* hierarchical structures were evaluated in neutral electrolyte (1.0 M phosphatic buffer solution, PBS, pH = 7) using a standard three-electrode system. As a comparison, commercially available benchmark IrO_2 electrocatalyst was also tested under the same condition. Before the lineal sweep voltammetry (LSV) test, the CoIr-*x* hierarchical structures were subjected to several cyclic voltammetry (CV) cycles at a sweep rate of 100 mV s^{-1} in the electrolyte until a stable CV curve was obtained. The LSV curves of the CoIr-*x* hierarchical structures were obtained at a scan rate of 10 mV s^{-1} with 95% *iR*-compensation. As shown in **Figure 3**a, the OER performance can be optimized by adjusting the concentration of Ir species. Specially, the CoIr-0.2 catalyst exhibits excellent OER activity in 1.0 M PBS with the lowest overpotential (η) of 373 mV required to achieve a current density (j) of 10 mA cm^{-2} from the LSV curves, which is 58 mV lower than that of commercial IrO_2 (431 mV @ j = 10 mA cm^{-2}). Meanwhile, the Tafel slope for CoIr-0.2 is calculated to be 117.5 mV dec^{-1}, which is much smaller than that of pure CoIr-0 (350.3 mV dec^{-1}) and IrO_2 (132.1 mV dec^{-1}) (Figure 3b). The lower η @ j = 10 mA cm^{-2} and Tafel slope values in 1.0 M PBS electrolyte suggest that the CoIr-0.2 requires a lower energy consumption for electrochemical processes. The excellent OER performance of CoIr-0.2 was further evaluated by measuring the electrochemical surface area via a CV method (Figure 3c and Figures S9–S12, Supporting Information). For comparison, the double layer capacitance (C_{dl}) of CoIr-0.2 (0.825 mF cm^{-2}) is higher than that of the CoIr-0 (0.332 mF cm^{-2}), CoIr-0.05 (0.439 mF cm^{-2}) and CoIr-0.1 (0.610 mF cm^{-2}), respectively, indicating the increasing of C_{dl} and exposing of more active sites, which is caused by Ir incorporation. Moreover, the excellent durability of CoIr-0.2 was also confirmed by chronopotentiometry test in 1.0 M PBS (Figure 3d). The excellent OER activity under neutral condition indicates that the CoIr-0.2 holds great potential for practical applications.

Besides neutral media, the CoIr-*x* samples were also evaluated in alkaline solution (1.0 M potassium hydroxide (KOH), pH = 14). Unsurprisingly, as the best OER electrocatalyst in neutral media, the CoIr-0.2 sample also requires the lowest η of 235 mV to reach a j of 10 mA cm^{-2} in 1.0 M KOH (Figure S13, Supporting Information), which is 45 mV lower than that of IrO_2 (280 mV @ j = 10 mA cm^{-2}), indicating that the CoIr-0.2 has a much better electrocatalytic OER activity than IrO_2. The Tafel plots of all the samples were also calculated from LSV curves to evaluate the OER catalytic kinetics (Figure S14, Supporting Information). The CoIr-0.2 displays a Tafel slope of 70.2 mV dec^{-1}, which is smaller than other CoIr-*x* samples, suggesting that the accelerated OH^- discharge process is the rate determining step.[39] Besides, the stability of the as-prepared CoIr-0.2 was performed by the chronopotentiometry measurement at a constant j of 10 mA cm^{-2} in 1.0 M KOH (Figure S15, Supporting Information). The result indicates that the CoIr-0.2 also shows excellent durability in alkaline. Due to the water

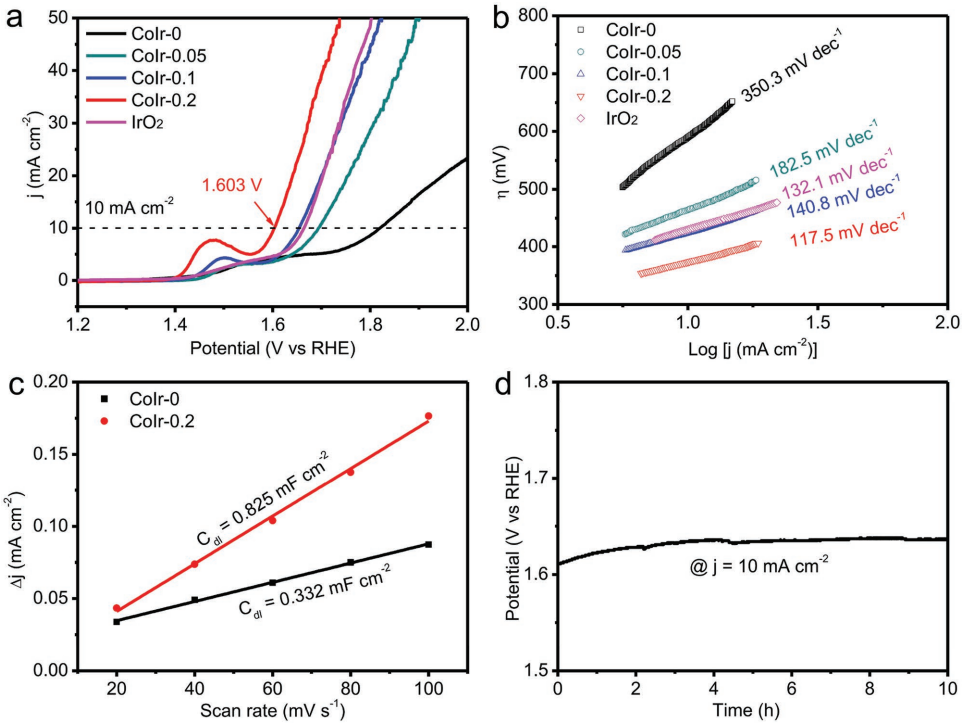

Figure 3. a) The *iR* corrected LSV curves and b) the corresponding Tafel plots of CoIr-*x* and IrO_2 samples in 1.0 M PBS. c) Charge current density differences ($\Delta j = j_{anodic} - j_{cathodic}$) plotted against scan rates of CoIr-0 and CoIr-0.2 samples. d) Chronopotentiometry curve of CoIr-0.2 in 1.0 M PBS at a constant current density of 10 mA cm^{-2}.

oxidation potential in alkaline media is much lower than that in neutral media,[40,41] the enhanced OER activity were measured in 1.0 M KOH in this work. These results demonstrate that the OER activity of CoIr-0.2 hierarchical structure is comparable to most of the state-of-the-art electrocatalysts in both neutral and alkaline electrolytes (Tables S1 and S2, Supporting Information).

Furthermore, it was reported that the electrocatalyst would suffer irreversible oxidation and reconstruction during the OER process.[14,26,42,43] Most recently published articles reported that the activation of electrochemical oxidation of metallic electrocatalysts in alkaline media could greatly improve the OER activity in neutral media, compared with that of direct activation in neutral media.[23] Meanwhile, the increasing of pH leads to the generation of catalytically active sites, which can associate with greater OER activity.[41] Identifying the precise structure of the reconstruction-derived component is considered as the key to unravel the intrinsic mechanism,[26] but keeping as a great challenge. In this case, the CoIr-0.2 reconstruction-derived component was elaborately characterized by XRD, HAADF-STEM, and XAFS after the OER stability test for 10 h in alkaline solution. The XRD result indicates that the α-Co(OH)$_2$ phase was transformed into β-phase Co oxyhydroxide (β-CoOOH) (Figure S16, Supporting Information). The HAADF-STEM result confirms that the Ir species are remained in atomic dispersion in the sample (Figure S17, Supporting Information). As shown in **Figure 4**a, the intensity of the white line of the normalized XANES spectrum at

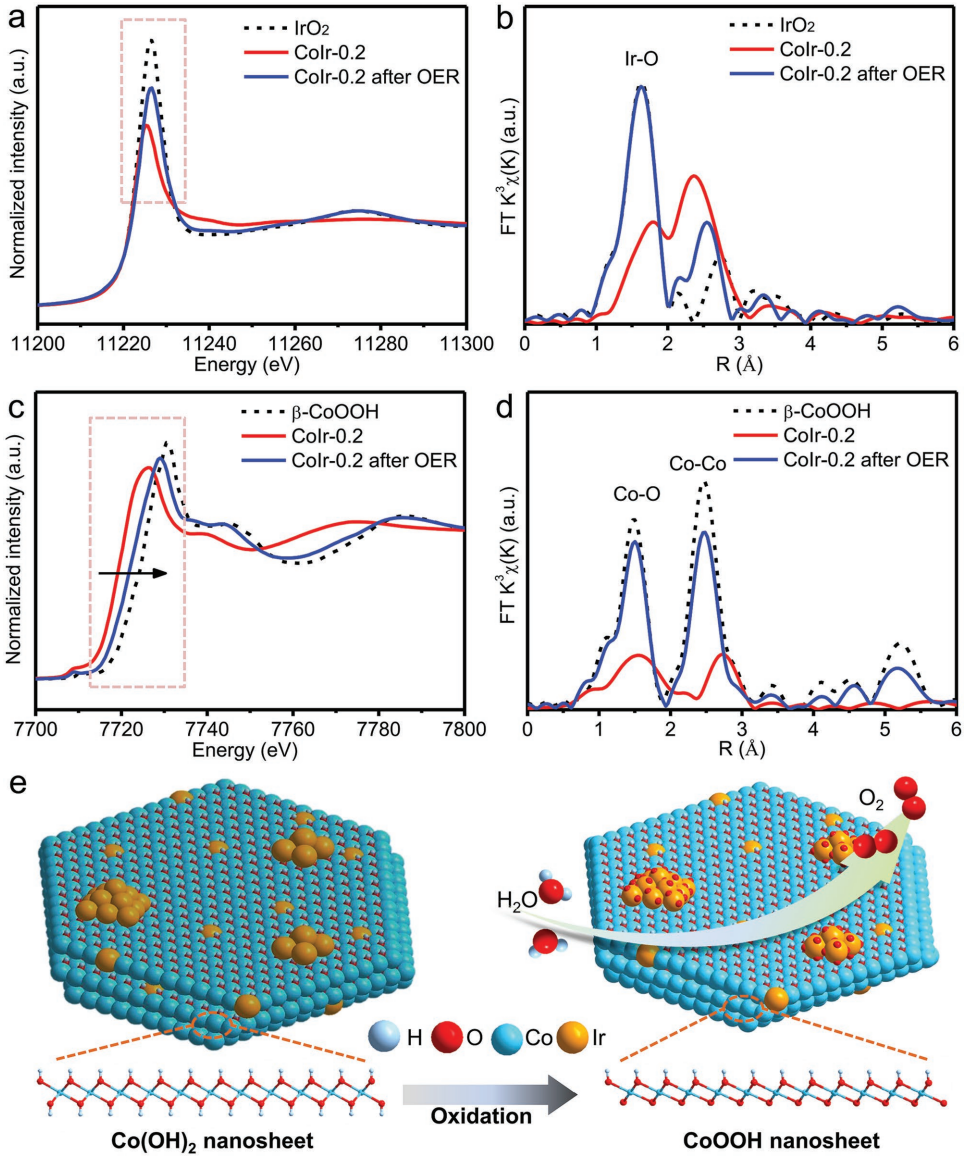

Figure 4. The XAFS characterizations of CoIr-0.2 after stability test for 10 h. a) The Ir L_3-edge XANES spectra and b) the corresponding FT curves. c) The Co K-edge XANES spectra and d) the corresponding FT curves. e) The mechanism diagram of OER on the CoIr-0.2 sample surface and the transformation of α-Co(OH)$_2$ to β-CoOOH phase.

Ir L_3-edge is obviously higher than that of the fresh CoIr-0.2, indicating that the oxidation state of Ir species was increased. The corresponding FT curve further confirms the oxidation of local structure of Ir atoms from the strong peak of Ir—O bond (Figure 4b). On the other hand, the white line of the normalized XANES spectrum at Co K-edge shows an evident shift to higher energy (Figure 4c), indicating that the Co species were oxidated into a higher valence. The corresponding FT curve is obviously changed and the nearest two main peaks at 1.50 and 2.49 Å corresponding to the Co—O and Co—Co coordinations in β-CoOOH,[44] respectively (Figure 4d). This result matches well with the XRD results (Figure S16, Supporting Information). Due to the poor crystalline and disordered structure, the α-$Co(OH)_2$ can rapidly transform into the more stable β-phase in alkaline media.[45] Therefore, the CoIr-0.2 is trend to be oxidized into β-phase CoOOH. These results are in consistent with recent reported electrocatalyst oxidation during the OER process to form IrO_2 and CoOOH.[34,45,46] Besides, the intensity of the two characteristic peaks of the CoIr-0.2 sample in FT curve are still lower than that of β-CoOOH reference in Figure 4d, implying the maintainment of unsaturated coordination of Co atoms. The similar conclusion can also be given from the characterization of the CoIr-0.2 reconstruction-derived component from neutral condition (Figure S18, Supporting Information). More importantly, the original defect-rich and low-coordination structure are beneficial for the formation of the real active site for the OER.[40,47] Thus, in this work, the defect-rich and low-coordination structure of the α-$Co(OH)_2$ hydroxide nanosheets combining with atomic Ir species are easy to convert into the real active sites for remarkably enhanced OER activity. The formed high valence Ir species and CoOOH with unsaturated coordination are known as efficient species for OER process.[40,44,48] The coexistence of Co and Ir would improve the orbital overlap with O-2p and thus facilitate the interaction with the intermediate adsorbates, leading to an optimized surface-oxygen interaction energy.[49] Based on the above analysis and the fact of the similar spatial structure of α-$Co(OH)_2$ and β-CoOOH, the models of OER on the CoIr-0.2 sample surface and the transformation of α-$Co(OH)_2$ to β-CoOOH phase are schematically represented in Figure 4e.

In summary, we have presented a facile strategy at room-temperature to fabricate self-assembled CoIr-*x* hierarchical structures consisting of flexible CoIr hydroxide nanosheets as efficient electrocatalyst toward OER in both neutral and alkaline conditions. The identified Ir atoms in ultrathin α-$Co(OH)_2$ nanosheets are bonded with adjacent Co atoms, leading to the formation of the Ir incorporated structures. The OER performance in both neutral and alkaline electrolytes demonstrates that the CoIr-*x* hierarchical structures represent the state-of-the-art OER catalysts. Most importantly, for the first time, we have provided elaborate structural identifications toward the OER reconstruction-derived component as actually catalytic sites and have found that the superior OER performance stemmed from unique low-coordination structure of the reconstruction-derived component. Considering the synthetic method and the excellent electrocatalytic OER performance, this work presents a promising alternative as highly efficient electrocatalyst for OER. The new understanding for the typical oxidation reaction provides significant guidance for the mechanistic insights in electrocatalytic field.

Experimental Section

Chemicals: Cobalt (II) nitrate hexahydrate ($Co(NO_3)_2{\cdot}6H_2O$, 98.5%), iridium (III) trichloride hydrate ($IrCl_3{\cdot}xH_2O$, 99.9%, metals basis), and iridium (IV) oxide (IrO_2, 99.9%) were purchased from Aldrich Chemical. KOH (85%), sodium borohydride ($NaBH_4$, >99%), and ethanol (C_2H_5OH, >99.7%) were obtained from Sinopharm Chemical Reagent. Nafion solution (5 wt%) were purchased from Alfa Aesar. All the chemicals were used as purchased without further purification. The water used in all experiments was deionized water (DIW).

Synthesis of Self-Assembled 3D CoIr-x Hierarchical Structures: In a typical preparation of self-assembled 3D CoIr-0.2 hierarchical structures, $Co(NO_3)_2{\cdot}6H_2O$ (1 mmol, 291 mg) and $IrCl_3{\cdot}xH_2O$ (0.2 mmol, 29.9 mg) were dissolved in DIW (100 mL) under vigorous stirring for 30 min to complete dissolution at room temperature. Subsequently, $NaBH_4$ solution (5 mL, 0.5 mol L^{-1}) was added and continuously stirred for 60 min. The resulting products were collected by centrifuging at 8000 rpm for 10 min and washed with ethanol and DIW for several times. After freeze drying, the samples were collected for further characterizations. The as-synthesized 3D CoIr hierarchical structures samples were denoted as CoIr-*x*, where *x* corresponding to the Ir/Co molar ratio in precursor (*x* = 0, 0.05, 01, and 0.2). The contrast sample (CoIr-0) was prepared by the same method except for the adding of $IrCl_3{\cdot}xH_2O$.

Characterizations: Powder XRD studies of the as-synthesized samples were carried out on a Philips X'Pert Pro Super X-ray diffractometer with Cu-K_α radiation (λ = 1.54178 Å). The morphological studies of the samples were characterized by using JEOL JSM 6700F field emission scanning electron microscope (SEM) and JEOL JEM 2010 TEM equipped with an energy-dispersive X-ray spectrometer (Oxford Instruments) for elemental mapping. XPS measurements were undertaken on Thermo ESCALAB 250Xi using Al K_α ($h\nu$ = 1486.6 eV) as the excitation source. The binding energies of XPS spectral range were calibrated for specimen charging effects using the C 1s level at the energy of 284.6 eV as a reference. All the XPS spectra were fitted and analyzed using XPSPEAK software with a Gaussiane–Lorentzian function and a nonlinear Shirley background. The Ir L_3-edge XAFS spectra were carried in fluorescence mode at the 1W1B beamline station of the Beijing Synchrotron Radiation Facility (BSRF). The Co K-edge XAFS spectra were measured in transmission mode at the BL14W1 beamline station of the Shanghai Synchrotron Radiation Facility (SSRF). The acquired XAFS data were processed according to the standard procedures using the ATHENA module implemented in the IFEFFIT software packages.[50]

Electrochemical Tests: All electrochemical measurements were performed using a three-electrode system on a CHI760e workstation (Shanghai Chenhua, China) at room temperature. First, the catalyst ink was prepared by ultrasonically dispersing the mixture of 4 mg of the as-synthesized catalyst, 460 µL of ethanol and 40 µL of 5 wt% Nafion solutions. Next, 5 µL of the catalyst ink was carefully dropped onto the polished glassy carbon electrode (GCE, 3 mm in diameter), followed by drying in air leading to a desirable catalyst loading (with the mass loading of 0.566 mg cm^{-2}). The GCE coated with the catalyst ink was served as the working electrode, a platinum mesh electrode as the counter electrode, and Ag/AgCl double junction electrode as the reference electrode. For comparison, IrO_2 with the similar mass loading was conducted for the same electrochemical tests. The electrochemical potentials measured against the Ag/AgCl reference electrode were converted to the reversible hydrogen electrode (RHE) scale via the Nernst equation: $E_{RHE} = E_{Ag/AgCl} + 0.059 \times pH + 0.197$, and the overpotential (η) for OER was calculated using the following equation: $\eta = E_{RHE}$–1.23 V.

Linear sweep voltammetry (LSV) is employed to obtain polarization curves of all the as-synthesized samples. Before the LSV measurement, the catalyst was subjected to a number of CV cycles at a scan rate of 100 mV s^{-1} until a stable CV curve was obtained. All the LSV data were measured at a scan rate of 10 mV s^{-1} and corrected with 95% *iR*-compensation. The long-term catalytic stability was recorded by a chronopotentiometry measurement at a constant *j* of 10 mA cm^{-2}. The

Tafel plots were derived from the OER LSV curves and calculated based on the equation $\eta = b \log j + a$, where b and j are the Tafel slope and current density, respectively. The electrochemical active surface areas were determined by taking CV measurement in the potential windows of 0.9–1.0 V versus RHE under different scan rates ranging from 20 to 100 mV s^{-1} with an interval point of 20 mV s^{-1}. The double layer capacitance (C_{dl}) was calculated by plotting the charge current density differences ($\triangle j = j_{anodic} - j_{cathodic}$) at 0.95 V versus RHE against the scan rate. The slope of the fitting line is equal to twice of the C_{dl}.

Supporting Information

Supporting Information is available from the Wiley Online Library or from the author.

Acknowledgements

Y.Z. and C.W. contributed equally to this work. This work was financially supported by Ministry of Science and Technology of China (2017YFA0303500 and 2014CB848900), National Natural Science Foundation of China (NSFC) (U1532112, 11574280, 11605201, and 21706248), Innovative Research Groups of NSFC (11621063), Chinese Academy of Sciences (CAS) Key Research Program of Frontier Sciences (QYZDB-SSW-SLH018), China Postdoctoral Science Foundation (BH2310000033), CAS Interdisciplinary Innovation Team, Innovative Program of Development Foundation of Hefei Center for Physical Science (T6FXCX003). L.S. acknowledges the recruitment program of global experts, the CAS Hundred Talent Program, Key Laboratory of Advanced Energy Materials Chemistry (Ministry of Education) Nankai University (111 project, B12015). The authors thank the Shanghai synchrotron Radiation Facility (14W1, SSRF), the Beijing Synchrotron Radiation Facility (1W1B and soft-X-ray endstation, BSRF), the Hefei Synchrotron Radiation Facility (Photoemission, Magnetic Circular Dichroism and Catalysis/Surface Science Endstations, Endstations at National Synchrotron Radiation Laboratory), the University of Science and Technology of China Center for Micro and Nanoscale Research and Fabrication for helps in characterizations.

Conflict of Interest

The authors declare no conflict of interest.

Keywords

atomic iridium, cobalt hydroxide, neutral electrolyte, oxygen evolution reaction, X-ray absorption spectra

Received: December 24, 2017
Revised: February 8, 2018
Published online:

[1] P. F. Liu, X. Li, S. Yang, M. Y. Zu, P. Liu, B. Zhang, L. Zheng, H. Zhao, H. G. Yang, *ACS Energy Lett.* **2017**, *2*, 2257.
[2] S. Nandi, S. K. Singh, D. Mullangi, R. Illathvalappil, L. George, C. P. Vinod, S. Kurungot, R. Vaidhyanathan, *Adv. Energy Mater.* **2016**, *6*, 1601189.
[3] G. Liu, P. Li, G. Zhao, X. Wang, J. Kong, H. Liu, H. Zhang, K. Chang, X. Meng, T. Kako, J. Ye, *J. Am. Chem. Soc.* **2016**, *138*, 9128.
[4] B. Zhang, X. Zheng, O. Voznyy, R. Comin, M. Bajdich, M. García-Melchor, L. Han, J. Xu, M. Liu, L. Zheng, F. P. García de Arquer, C. T. Dinh, F. Fan, M. Yuan, E. Yassitepe, N. Chen, T. Regier, P. Liu, Y. Li, P. De Luna, A. Janmohamed, H. L. Xin, H. Yang, A. Vojvodic, E. H. Sargent, *Science* **2016**, *352*, 333.
[5] J. Suntivich, K. J. May, H. A. Gasteiger, J. B. Goodenough, Y. Shao-Horn, *Science* **2011**, *334*, 1383.
[6] H. Liang, F. Meng, M. Cabán-Acevedo, L. Li, A. Forticaux, L. Xiu, Z. Wang, S. Jin, *Nano Lett.* **2015**, *15*, 1421.
[7] X. Long, J. Li, S. Xiao, K. Yan, Z. Wang, H. Chen, S. Yang, *Angew. Chem.* **2014**, *126*, 7714.
[8] W. Li, X. Gao, D. Xiong, F. Wei, W. G. Song, J. Xu, L. Liu, *Adv. Energy Mater.* **2017**, *7*, 1602579.
[9] A. Grimaud, O. Diaz-Morales, B. Han, W. T. Hong, Y.-L. Lee, L. Giordano, K. A. Stoerzinger, M. T. M. Koper, Y. Shao-Horn, *Nat. Chem.* **2017**, *9*, 457.
[10] S. Zhao, Y. Wang, J. Dong, C.-T. He, H. Yin, P. An, K. Zhao, X. Zhang, C. Gao, L. Zhang, J. Lv, J. Wang, J. Zhang, A. M. Khattak, N. A. Khan, Z. Wei, J. Zhang, S. Liu, H. Zhao, Z. Tang, *Nat. Energy* **2016**, *1*, 16184.
[11] H. Liu, Q. He, H. Jiang, Y. Lin, Y. Zhang, M. Habib, S. Chen, L. Song, *ACS Nano* **2017**, *11*, 11574.
[12] H. Jiang, Y. Yao, Y. Zhu, Y. Liu, Y. Su, X. Yang, C. Li, *ACS Appl. Mater. Interfaces* **2015**, *7*, 21511.
[13] A. Yu, C. Lee, M. H. Kim, Y. Lee, *ACS Appl. Mater. Interfaces* **2017**, *9*, 35057.
[14] B. Song, K. Li, Y. Yin, T. Wu, L. Dang, M. Cabán-Acevedo, J. Han, T. Gao, X. Wang, Z. Zhang, J. R. Schmidt, P. Xu, S. Jin, *ACS Catal.* **2017**, *7*, 8549.
[15] X. Yan, Y. Jia, J. Chen, Z. Zhu, X. Yao, *Adv. Mater.* **2016**, *28*, 8771.
[16] L. Xu, Q. Jiang, Z. Xiao, X. Li, J. Huo, S. Wang, L. Dai, *Angew. Chem., Int. Ed.* **2016**, *55*, 5277.
[17] G. Zhang, S. Zang, X. Wang, *ACS Catal.* **2015**, *5*, 941.
[18] J. Del-Pilar, B. Wang, P. K. Dutta, *Microporous Mesoporous Mater.* **2015**, *217*, 125.
[19] K. Maeda, K. Ishimaki, Y. Tokunaga, D. Lu, M. Eguchi, *Angew. Chem., Int. Ed.* **2016**, *55*, 8309.
[20] K. Li, J. Zhang, R. Wu, Y. Yu, B. Zhang, *Adv. Sci.* **2016**, *3*, 1500426.
[21] L. Zhang, L. Xie, M. Ma, F. Qu, G. Du, A. M. Asiri, L. Chen, X. Sun, *Catal. Sci. Technol.* **2017**, *7*, 2689.
[22] L. Yang, D. Liu, S. Hao, R. Kong, A. M. Asiri, C. Zhang, X. Sun, *J. Mater. Chem. A* **2017**, *5*, 7305.
[23] K. Xu, H. Cheng, L. Liu, H. Lv, X. Wu, C. Wu, Y. Xie, *Nano Lett.* **2016**, *17*, 578.
[24] M. Schreier, L. Curvat, F. Giordano, L. Steier, A. Abate, S. M. Zakeeruddin, J. Luo, M. T. Mayer, M. Grätzel, *Nat. Commun.* **2015**, *6*, 7326.
[25] X. Zheng, B. Zhang, P. De Luna, Y. Liang, R. Comin, O. Voznyy, L. Han, F. P. García de Arquer, M. Liu, C. T. Dinh, T. Regier, J. J. Dynes, S. He, H. L. Xin, H. Peng, D. Prendergast, X. Du, E. H. Sargent, *Nat. Chem.* **2018**, *10*, 149.
[26] E. Fabbri, M. Nachtegaal, T. Binninger, X. Cheng, B.-J. Kim, J. Durst, F. Bozza, T. Graule, R. Schäublin, L. Wiles, M. Pertoso, N. Danilovic, K. E. Ayers, T. J. Schmidt, *Nat. Mater.* **2017**, *16*, 925.
[27] K. Lee, L. Zhang, J. Zhang, *J. Power Sources* **2007**, *170*, 291.
[28] Y. Pi, Q. Shao, P. Wang, J. Guo, X. Huang, *Adv. Funct. Mater.* **2017**, *27*, 1700886.
[29] J. Feng, F. Lv, W. Zhang, P. Li, K. Wang, C. Yang, B. Wang, Y. Yang, J. Zhou, F. Lin, C.-C. Wang, S. Guo, *Adv. Mater.* **2017**, *29*, 1703798.
[30] H. Fan, X. Huang, L. Shang, Y. Cao, Y. Zhao, L. Z. Wu, C. H. Tung, Y. Yin, T. Zhang, *Angew. Chem., Int. Ed.* **2016**, *55*, 2167.
[31] M. Zhu, Q. Shao, Y. Pi, J. Guo, B. Huang, Y. Qian, X. Huang, *Small* **2017**, *13*, 1701295.
[32] Z.-P. Zhang, X.-Y. Wang, K. Yuan, W. Zhu, T. Zhang, Y.-H. Wang, J. Ke, X.-Y. Zheng, C.-H. Yan, Y.-W. Zhang, *Nanoscale* **2016**, *8*, 15744.
[33] T. Xue, X. Wang, J.-M. Lee, *J. Power Sources* **2012**, *201*, 382.

[34] H. Jin, S. Mao, G. Zhan, F. Xu, X. Bao, Y. Wang, *J. Mater. Chem. A* **2017**, *5*, 1078.
[35] T. Higaki, H. Kitazawa, S. Yamazoe, T. Tsukuda, *Nanoscale* **2016**, *8*, 11371.
[36] L. He, Y. Huang, X. Y. Liu, L. Li, A. Wang, X. Wang, C.-Y. Mou, T. Zhang, *Appl. Catal., B* **2014**, *147*, 779.
[37] J. Yang, D. He, W. Chen, W. Zhu, H. Zhang, S. Ren, X. Wang, Q. Yang, Y. Wu, Y. Li, *ACS Appl. Mater. Interfaces* **2017**, *9*, 39450.
[38] Y. Liu, H. Cheng, M. Lyu, S. Fan, Q. Liu, W. Zhang, Y. Zhi, C. Wang, C. Xiao, S. Wei, B. Ye, Y. Xie, *J. Am. Chem. Soc.* **2014**, *136*, 15670.
[39] Z. H. Xue, H. Su, Q. Y. Yu, B. Zhang, H. H. Wang, X. H. Li, J. S. Chen, *Adv. Energy Mater.* **2017**, *7*, 1602355.
[40] A. Grimaud, A. Demortiere, M. Saubanere, W. Dachraoui, M. Duchamp, M.-L. Doublet, J.-M. Tarascon, *Nat. Energy* **2017**, *2*, 16189.
[41] K. A. Stoerzinger, R. R. Rao, X. R. Wang, W. T. Hong, C. M. Rouleau, Y. Shao-Horn, *Chemistry* **2017**, *2*, 668.
[42] F. Hu, S. Zhu, S. Chen, Y. Li, L. Ma, T. Wu, Y. Zhang, C. Wang, C. Liu, X. Yang, L. Song, X. Yang, Y. Xiong, *Adv. Mater.* **2017**, *29*, 1606570.
[43] D. Li, H. Baydoun, C. N. Verani, S. L. Brock, *J. Am. Chem. Soc.* **2016**, *138*, 4006.
[44] J. Huang, Q. Shang, Y. Huang, F. Tang, Q. Zhang, Q. Liu, S. Jiang, F. Hu, W. Liu, Y. Luo, T. Yao, Y. Jiang, Z. Pan, Z. Sun, S. Wei, *Angew. Chem., Int. Ed.* **2016**, *55*, 2137.
[45] T. Deng, W. Zhang, O. Arcelus, J.-G. Kim, J. Carrasco, S. J. Yoo, W. Zheng, J. Wang, H. Tian, H. Zhang, X. Cui, T. Rojo, *Nat. Commun.* **2017**, *8*, 15194.
[46] Y. Pi, N. Zhang, S. Guo, J. Guo, X. Huang, *Nano Lett.* **2016**, *16*, 4424.
[47] S. Gao, Y. Sun, F. Lei, L. Liang, J. Liu, W. Bi, B. Pan, Y. Xie, *Angew. Chem., Int. Ed.* **2014**, *53*, 12789.
[48] J. Huang, J. Chen, T. Yao, J. He, S. Jiang, Z. Sun, Q. Liu, W. Cheng, F. Hu, Y. Jiang, Z. Pan, S. Wei, *Angew. Chem., Int. Ed.* **2015**, *54*, 8722.
[49] W. Q. Zaman, Z. Wang, W. Sun, Z. Zhou, M. Tariq, L. Cao, X.-Q. Gong, J. Yang, *ACS Energy Lett.* **2017**, *2*, 2786.
[50] B. Ravel, M. Newville, *J. Synchrotron Radiat.* **2005**, *12*, 537.